Ocean air masses dominate the land-surface atmospheric water cycles in the coastal areas of Liaodong Bay: Insights from stable isotopes

Yi-Yuan Du[1,2*], Ri-Hong Wen[3*], Shristee Panthee[1], Sissou Zakari[6], Liang Song[1], Wen-Jie Liu[1], Bin Yang[1†]

[1]CAS Key laboratory of Tropical Forest Ecology, Xishuangbanna Tropical Botanical Garden, Chinese Academy of Sciences, Menglun 666303, Yunnan, China.

[2]University of Chinese Academy of Sciences, Beijing 100049, China.

[3]Institute of Atmospheric Environment, China Meteorological Administration, Shenyang, 110166, Liaoning, China.

[4]Laboratory of Hydraulics and Environmental Modeling, Facult´e d'Agronomie, Universit´e de Parakou, Parakou, 03 BP 351, Benin.

Corresponding author:Yang Bin (yangbin@xtbg.ac.cn)

Menglun Yunnan, China； Tel.: 19969108917; Fax: 86-691-8715070

Key Points:

- Spatial-temporal variations of water vapor isotopes are very different during 2019/2020 growing (May-September) seasons.
- Meteorological variables are not reliable indicators for water vapor $\delta^{2}H$, $\delta^{18}O$, and d-excess at Panjin experimental station.
- Ocean air masses from East Asian monsoon dominate land-surface atmospheric water vapor cycles in the coastal areas of Liaodong Bay.

Abstract

Long-term atmospheric water vapor hydrogen (δ^2H), oxygen (δ^{18}O), and deuterium excess (*d-excess*) can provide unique insights into the land-atmosphere coupling processes. The in-situ measurements of atmospheric water vapor δ^2H, δ^{18}O, and *d-excess* were conducted above a reed wetland of Liaodong Bay (2019-2020). We found significant inter-annual variations in atmospheric water vapor isotopes between the two growing (May-September) seasons. The δ^2H, δ^{18}O, and *d-excess* of atmospheric water vapor exhibited different seasonal and diurnal cycles respect to the vertical (i.e., 1 m, 3 m, and 5 m) measurement heights, especially in 2019. The isotopic differences of atmospheric water vapor among vertical measurement heights were more evident in the daytime (8:00-20:00 LST) than at night (20:00-8:00 LST). Rainfall events had a direct impact on the diurnal patterns of water vapor isotopes, and the influences depended on rainfall intensities. However, only week correlations existed between water vapor isotopes and local meteorological factors (R^2 = 0.01-0.16, P < 0.001), such as water vapor concentration (w), relative humidity (RH), and surface air temperature (T_a). Based on the back-air trajectory analyses, the spatial-temporal dynamics of atmospheric water vapor isotopes highly synchronized with monsoon activities. The dominant air masses in this region mainly arose from ocean sources, which contributed to 62.1 ± 12.2% (49.4-84.5%) of the total air moisture. High *d-excess* consistently followed the strong monsoon activities, suggesting predominating impacts of ocean air masses from the East Asian monsoon region. High-resolution measurements of atmospheric water vapor isotopes will improve our understanding of the hydrological cycles in coastal areas.

Plain Language Summary

The coastal wetland regions in East Asia always have complex atmospheric hydrological processes, because they are influenced both by the westerly belt and the East Asian monsoon. Under such circumstances, still the question remains how do the multiple air masses affect the seasonal and diurnal patterns of atmospheric circulations? We implemented high temporal resolution (1Hz) measurements of atmospheric hydrogen (HDO/$H_1H_2{}^{18}O$) and oxygen ($H_2{}^{18}O$ and $H_2{}^{16}O$) using an off-axis integrated cavity output spectroscopy (OA-ICOS) technology in a reed wetland. The deuterium excess (*d-excess* = $\delta^2H - 8 \times \delta^{18}O$) of atmospheric water vapor was further used as an indicator for identifying the moisture source locations (2019-2020). There were obvious seasonal and diurnal variations of atmospheric water vapor δ^2H, δ^{18}O, and *d-excess*. However, the inter-annual variations in atmospheric water vapor isotopes were more notable in this study, mainly due to the stronger monsoon activities. For example, the landing of typhoon "Lekima" brought a very high level of atmospheric water vapor *d-excess* in 2019. Therefore, the local meteorological variables might not be sufficient predictors of the atmospheric water vapor isotopes in the coastal wetland regions.

1 Introduction

Measurements of atmospheric water vapor hydrogen (δ^2H), oxygen (δ^{18}O), and deuterium excess (*d-excess*) can provide unique insights into the land-atmosphere coupling processes (Gat, 1996; Lee et al., 2005; Vuille et al., 2003). The δ^2H, δ^{18}O, and *d-excess* of water vapor (termed as the δ_{vapor} hereafter) can be used as natural tracers of atmospheric water cycles (Bastrikov et al., 2014; Christner et al., 2017; Munksgaard et al., 2020; Wen et al., 2008, 2010). Influenced by lower tropospheric water variations (e.g., precipitation and vertical atmospheric mixing) and local vegetation properties (e.g., soil evaporation and plant transpiration), the signatures of land-surface water vapor δ_{vapor} contain subtle information concerning water movements between the atmospheric boundary layer (ABL) and Earth's surfaces (Huang & Wen, 2014; Laonamsai et al., 2021; Lee et al., 2006). Thus, there is a growing interest in high-resolution measurements of atmospheric water vapor δ_{vapor} from ecosystem to regional scales (Galewsky et al., 2016; Steen-Larsen et al., 2013; Wei & Lee, 2019). Several studies have successfully completed the in-situ atmospheric water vapor δ_{vapor} monitoring based on the technological advantages of laser spectrometers (Aemisegger et al., 2014; Hu et al., 2014; Noone et al., 2012). However, it is still necessary to conduct in-situ measurements of atmospheric water vapor δ_{vapor} above near-surface ecosystems (Galewsky et al., 2016; Lee et al., 2005, 2007), compared with the condensed water isotopes that have formed a well-known global network (e.g., Global Network of Isotopes in Precipitation, GNIP).

To the best of our knowledge, datasets of in-situ atmospheric water vapor δ_{vapor} are reported across 49 sites worldwide. Those sites reflect the global land surface in all forms, including oceans (e.g., Bonne et al., 2019; Galewsky et al., 2022; Steen-Larsen et al., 2014a), forests (Aron et al., 2019; Bastrikov et al., 2014; Mercer et al., 2020), grasslands (Hu et al., 2014; Parkes et al., 2017; Tremoy et al., 2014), croplands (Griffis et al., 2016; Huang & Wen, 2014; Wen et al., 2012), ice sheets (Bonne et al., 2020; Casado et al., 2016; Steen-Larsen et al., 2014b), cities (Christner et al., 2017; Noone et al., 2012; Wang et al., 2021), and lakes (Cui et al., 2018; Hu et al., 2021; Xiao et al., 2017). These studies confirm the great potential of in-situ water vapor δ_{vapor} measurements to deconstruct the complex hydrological processes. However, among the available data on atmospheric water vapor δ_{vapor}, the data from coastal wetlands are scarce (Delattre et al., 2015; Lai et al., 2018). For example, Delattre et al. (2015) showed that ground level atmospheric vapour composition can record both local and regional isotopic signatures during 36 consecutive summer days . The water vapor δ_{vapor} data reported by Lai et al. (2018) showed that, on daily time scales (11-28 July, 2017), substantial rain recycling and large-scale atmospheric water transport occur above a coastal mangrove forest in southern China, which is subjected to the monsoons from South China Sea, Indian Ocean, Pacific Ocean, and local land areas. Nevertheless, the brief campaigns of water vapor δ_{vapor} measurements would restrain the best demonstration of atmospheric processes in the coastal wetlands.

Previous studies have demonstrated that the small spatial and temporal variations of atmospheric water vapor δ_{vapor} are affected mainly by processes of atmospheric entrainments, land surface evapotranspiration (i.e., soil evaporation and plant transpiration, ET), and vapor condensations (Huang & Wen, 2014; Lee et al., 2007; Fiorella et al., 2019; Diekmann et al., 2021). Entrainment processes of the free atmosphere will vertically deplete the ^{2}H and ^{18}O of water vapor near the land surfaces (Devi et al., 2014; Kurita et al., 2012; Wei et al., 2015). Local ET will enrich the ^{2}H and ^{18}O of near-surface atmosphere above the densely vegetated landscapes, which usually plays a dominant role in the variations of water vapor δ_{vapor} (Lai & Ehleringer, 2011; Zhang et al., 2011). The diurnal dynamics of atmospheric water vapor δvapor are closely associated with the vapor condensation processes (e.g., precipitation, dew and fog), which is mainly caused by the equilibrium phase changes of local water vapor during the synoptic events (Bailey et al., 2015; Farlin et al., 2013; Wen et al., 2012). On large spatial scales, air mass advection is considered as a critical factor contributing to the temporal variability in atmospheric water vapor δ_{vapor} (Dahinden et al., 2021; Galewsky et al., 2011; Steen-Larsen et al., 2015).

Despite high-resolution monitoring efforts over the past two decades, decoupling the atmospheric water vapor δ_{vapor} variability across various timescales remains challenging (Bagheri et al., 2019; Berkelhammer et al., 2013; Lee et al., 2005; Dahinden et al., 2021). The deuterium excess (*d-excess* = $\delta^{2}H - 8 \times \delta^{18}O$) of atmospheric water vapor provides a new insight into the source identification of atmospheric moistures (Dansgaard, 1964; Merlivat & Jouzel, 1979; Welp et al., 2012). The theoretical basis of this application is that the *d-excess* of water vapor is closely linked to the environmental conditions during the kinetic fractionation processes (Araguas-Araguas et al., 2000; Craig, 1961). Hence, the strong sensitivity of *d-excess* to local atmosphere relative humidity (RH) can place better constraints on the water transport processes than the analyses of water vapor $\delta^{2}H$ and $\delta^{18}O$ alone (Lai et al., 2018; Wei & Lee, 2019). Previous work has traced both the ocean moisture sources (Dahinden et al., 2021; Gonzalez et al., 2016; Salamalikis et al., 2015) and continental moisture recycling (Aemisegger et al., 2014; Fiorella et al., 2019). To better resemble the transmission path of large-scale air masses, tools of Hybrid Single-Particle Lagrangian Integrated Trajectory (HYSPLIT) and TrajStat models have been widely used in conjunction with water vapor isotopes in recent years (Bagheri et al., 2019; Fiorella et al., 2018; Gonzalez et al., 2016; Salamalikis et al., 2015). It is foreseeable that long-term water vapor d-excess measurements will improve our understanding of atmospheric processes and the associated mechanisms in the coastal wetlands.

Liaodong Bay, a high-latitude continental bay (37.1-41.0° N, 117.6-121.2° E), has the largest size and northernmost semi-enclosed seaports in China. It contains a wetland area of approximately 5300 km^2 (Luo et al., 2021). According to the 2nd National Wetland Survey Statistics Report (NFGA, 2010), the reed wetlands in this region are well-preserved and among the largest in extent (~ 2500 km^2) in the world. Those offshore wetlands are located in the transition zones between continents and oceans, which are vulnerable to natural and anthropogenic activities, such as urban

and agricultural runoff. To fill the gaps in knowledge regarding the mechanisms of water cycle processes, we conducted two-year (2019-2020) measurements of atmospheric water vapor δ^2H, δ^{18}O, and *d-excess* in the reed wetlands of Liaodong Bay. The present study aims to (i) investigate the spatial-temporal dynamics of atmospheric water vapor isotopes above the coastal wetland, and (ii) identify the contributing factors that affect the isotopic characteristics of atmosphere in Liaodong Bay. We hypothesize that (1) isotopic gradients exist for atmospheric water vapor measurements along the monitoring heights due to the growth of reeds, and (2) moist air masses from the East Asian monsoon strongly affects the atmospheric water vapor isotopes.

2 Materials and Methods

2.1 Study site

The observations were carried out at Panjin Wetland Field Science Experimental Station (40° 56′ 40″ N, 121° 56′ 36″ E, and elevation 2.1 m), located in the north of Liaodong Bay. This station is a member of the National Climatic Observatory of China Meteorological Administration (CMA), which is adjacent to the Liaohe River Delta wetlands, and 12 km to the Bohai Sea (Figure 1a and 1b). This area is characterized by the semi-humid temperate monsoon climate, influenced by the westerly belt and the East Asian monsoon. The southwest East Asian monsoon prevails from May to September, which brings abundant rainfall between July and September (Huang et al., 2018). The regional meteorological records (1961-2010) indicate that the mean air temperature and annual precipitation are 9.1 ℃ and 643.9 mm, respectively. Approximately 170 days of frost-free weather occur throughout the year. The annual evaporation is about 516.0-720.3 mm (2012-2015). The research site (150 m × 150 m) is situated in the center of a reed marsh (~ 780 km2), with a vegetation coverage of more than 90% (Wang et al., 2016). Meteorological data of surface air temperature (T_a), relative humidity (RH), and total precipitation (P) obtained from an automatic weather station (Model A753WS, Adcon Telemetry Inc., Santa Rosa, CA). The leaf area index (LAI) and height of the reeds were collected for fifteen days intervals during the growing season (May-September). During the study periods of 2019 and 2020, the maximum LAI and maximum height were 5.1 m^2 m^{-2} and 2.5 m, respectively.

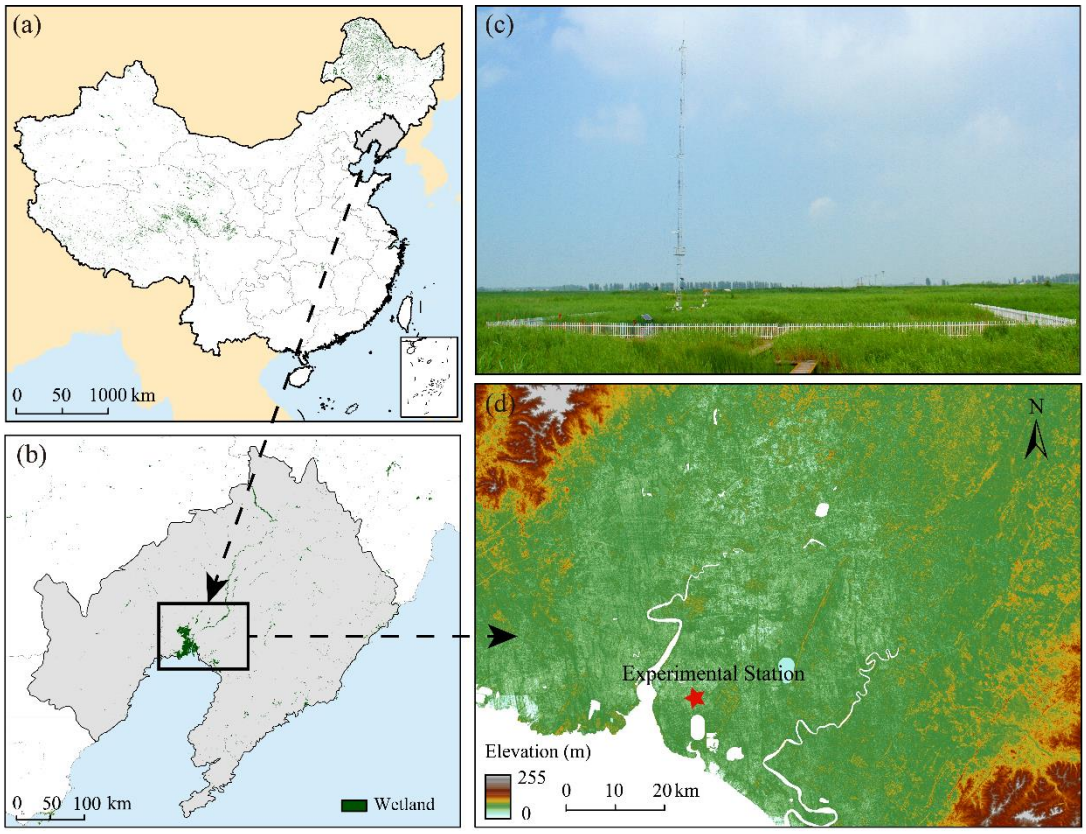

Figure 1. Maps showing the locations of Liaodong Bay (**a**, **b**) and Panjin experimental station (**c**, **d**) in this study. Elevation data was downloaded from the National Earth System Science Data Center, National Science & Technology Infrastructure of China (http://www.geodata.cn).

2.2 In-Situ measurement of water vapor isotopes

The in-situ system used to measure the atmospheric water vapor δ^2H and $\delta^{18}O$ consisted of a water vapor isotope analyzer (WVIA), a water vapor isotope standard source (WVISS), and an air sampling system (ASS). The WVIA was used to measure water vapor isotopes (at a frequency of 1 Hz) based on the off-axis integrated cavity output spectroscopy (OA-ICOS; Model TIWA-912, Los Gatos Research, Mountain View, CA, USA). The analyzer has a near-infrared diode laser scanning absorption lines (~ 1.4 μb) for $H_2{}^{16}O$, $H_2{}^{18}O$, and $H_1H_2{}^{16}O$ (HDO), whose precision was approximately 0.4‰ for δ^2H and 0.08‰ for $\delta^{18}O$ (Steen-Larsen et al., 2013; Wen et al., 2012). The WVISS is an online calibration device that generates fixed concentrations of continuous vapor streams (Model 908-004-902, Los Gatos Research, Mountain View, CA, USA). In this study, ultrapure liquid water with known isotopic values was nebulized (at a rate of 2-10 L min^{-1}) to produce three designated gradients of standard streams (S_1, S_2, and S_3, 300s each) covering the water vapor concentration of ambient air. There is no isotopic fractionation since the nebulizer and hot chamber (2 L) of WVISS will ensure instant evaporation (heated to 80 °C) of all liquid water. The ASS was mounted on a 30 m height tower (Figure 1c) and used to pump ambient air from four heights (1, 3, 10, and 15 m) with 300s spent

on each height. To reduce the residence time of ambient air in the inlet lines (i.e., "memory effects"), the sampling lines were pumped at approximately 2 L min^{-1} using a commercial multiplexer (Model MC-2000-8, Lica United Technology Limited Inc., Beijing, CHN). Teflon pipes were used in conjunction with individual heating tapes and jackets to prevent possible vapor condensation in the sampling tubes (Lee et al., 2005; Sturm & Knohl, 2010). Filters were installed at the entrances of the air-intake lines to prevent sucking liquid water into the instrument (Model 300-01961, LI-COR Inc., Lincoln, NE, USA). The switching sequence was S_1, S_2, S_3, and ambient air, with 15 minutes on the standard streams and 220 minutes on ambient air. The WVIA and WVISS were placed in an air-conditioning room to minimize the temperature-driven drifts.

While using the OA-ICOS for high-precision measurements of atmospheric water vapor δ^2H and $\delta^{18}O$, measurement bias can occur because of the instrumental concentration-dependence and time-drift (Bastrikov et al., 2014; Wen et al., 2008, 2012). Here, we followed a user-configurable "two-point calibration" protocol described by Wen et al. (2012), Huang & Wen (2014) and Xiao et al. (2017). Every 220 minutes (i.e., ~ 3.7 h) after the ambient (1, 3, 10, and 15 m) air measurements, two of the three standards (S_1, S_2, and S_3) spanning the water vapor concentration of ambient air were used to linearly calibrate atmospheric water vapor measurements. The isotopic values of the liquid calibration standards were measured using a liquid water isotope analyzer (Model GLA 431-TLWIA, Los Gatos Research, Mountain View, CA, USA), which were scaled to the Vienna Standard Mean Ocean Water (VSMOW) scale. For all the raw δ^2H and $\delta^{18}O$ measurements, the first 180 of 300 s spent measuring a given standard stream or an ambient vapor were discarded from the analysis to eliminate the possible memory effects. Then, the "two-point" linear interpolation was implemented using the following formula (Wen et al., 2012; Huang & Wen, 2014):

$$\delta_{vapor} = \delta_{s1} + \frac{(\delta_{s2} - \delta_{s1})}{(X_{s2} - X_{s1})} \times (X_{air} - X_{s1}) \quad (1)$$

where δ_{vapor} is the isotopic ratio ($^2H/^1H$, or $^{18}O/^{16}O$) of one ambient air (i.e., 1, 3, 10, and 15 m), δ_{s1} and δ_{s2} are the single-point corrected ambient airs that are normalized to a reference humidity (i.e., X_{s1} and X_{s2}), X_{s1}, X_{s2} and X_{s1} are water vapor concentrations of the two selected standard streams (S_1, S_2, and S_3) and the ambient air, respectively.

The isotopic data collected at 1 m, 3 m, and 15 m in height were used for representing the lower, middle, and upper canopy during the 2019-2020 growing (May-September) seasons. The second-order parameter deuterium excess (*d-excess* = $\delta^2H - 8 \times \delta^{18}O$) is defined as the deviation from the linear relationship between $^2H/^1H$ and $^{18}O/^{16}O$ in the Global Meteoric Water Line (GMWL) having a mean slope of 8 (Dansgaard, 1964; Merlivat & Jouzel, 1979). All data reported were block-averaged to hourly intervals.

2.3 Back-air mass trajectory analyses

The Hybrid Single Particle Lagrangian Integrated Trajectory (HYSPLIT) model was used to track changes in isotopic composition and moisture sources (Christner et al., 2018; Munksgaard et al., 2020). The HYSPLIT model (https://ready.arl.noaa.gov/HYSPLIT.php) was developed by the National Oceanic and Atmospheric Administration-Air Resources Laboratory (NOAA-ARL). Inputs of the HYSPLIT model include the cloud height, wind direction, temperature, and surface pressure, which are available from the Global Data Assimilation System (GDAS) meteorological data. In this study, the spatial resolution of the HYSPLIT model was set to 1° × 1°, and the starting height was set to 500 m above ground level. The 48-hour back-tracking analysis (close to the time that water vapor is present in the air) was performed hourly for the experimental site from May to September 2019 and 2020. The angular distance of the TrajStat model (http://www.meteothinker.com/downloads/index.html) was used to cluster the trajectories of air mass reaching the experimental station:

$$D = \frac{1}{n}\sum_{i=1}^{n}\left(0.5\,\frac{A_i+B_i-C_i}{\sqrt{A_iB_i}}\right) \tag{2}$$

where D is the average angular distance between two backward trajectories, A and B are the squares of the straight-line distances between the trajectory points and the experimental site, and C denotes the square of the straight-line distance between the two trajectory points.

The Concentration Weighted Trajectory (CWT) method was used to identify the potential source regions contributing to the variability of atmospheric water vapor *d-excess* at the experimental site (Li et al., 2020; Salamalikis et al., 2015). The rearward trajectories were assigned by the equally sized *i* × j grid cells. The sample concentrations accompanying trajectories that traversed each grid cell were averaged to provide each grid cell with a weighted concentration. The calculation of this method could be found in Li et al. (2020):

$$C_{ij} = \frac{1}{\sum_{l=1}^{M}\tau_{ijl}}\sum_{l=1}^{M} c_l\tau_{ijl} \tag{3}$$

where Cij is the average *d-excess* concentration in the ij^{th} cell, *l* is the trajectory index, *M* is the total number of the trajectories, cl is the concentration (*d-excess*) of the trajectory *l*, and τ_{ijl} is the time spent in the ij^{th} cell by the trajectory *l*. The weight function (W*ij*) was further introduced (WCWT*ij* = C*ij* × W*ij*) to reduce uncertainty because the error of CWT increases with the distance between the grid and the experimental station.

2.4 Statistical analyses

The isotopic data of atmospheric water vapor were calibrated based on the "two-point calibration" protocol using Matrix Laboratory (MATLAB, version 9.2.0, The MathWorks, Inc. Natick, USA). The normality and homogeneity of all data were checked using IBM SPSS statistical software (Version 22.0, SPSS Inc., Chicago, USA). One-way analysis of variance (ANOVA) and multiple means comparisons (LSD) were used to highlight differences in data between months and vertical strata. Considering the possible errors of the two variables, we used geometric mean regression (GMR) to assess the relationships between atmospheric water vapor isotopes and meteorological data with two probability levels of $P \leq 0.05$ and $P \leq 0.001$.

3 Results

3.1 Long time scale variations

Figure 2 shows the seasonal variations in hourly measured atmospheric water vapor δ^2H, $\delta^{18}O$, and *d-excess* at lower (1 m), middle (3 m), and upper (15 m) measurement heights during the 2019-2020 growing (May-September) seasons. The meteorological data of water vapor concentration (*w*), leaf area index (LAI), relative humidity (RH), total precipitation (P), and surface air temperature (T_a) are also presented for the Panjin experimental station. The WVIA analyzer was under repairs from June 20 to July 10, 2019, and from August 24 to September 9, 2020. For the rest of the study periods, only short gaps occurred in the in-situ measurements of atmospheric water vapor δ^2H, $\delta^{18}O$, and *d-excess* due to the occasional system downtimes (e.g., electricity interruption and/or analyzer breakdown). The monthly average of the above isotopic values of atmospheric water vapor and meteorological data are summarized in Table 1.

The δ^2H, $\delta^{18}O$, and *d-excess* of atmospheric water vapor underwent pronounced inter-annual and annual changes with months and vertical measurement heights (Figure 2). Significant differences existed in atmospheric water vapor δ^2H ($P < 0.001$), $\delta^{18}O$ ($P < 0.05$), and *d-excess* ($P < 0.001$) between 2019 and 2020. The mean isotopic values of atmospheric water vapor were higher in 2019 (δ^2H: − 108.4 ± 21.4‰, $\delta^{18}O$: − 16.64 ± 3.13‰, and *d-excess*: 26.3 ± 11.7‰) than in 2020 (− 120.7 ± 20.2‰, − 16.98 ± 2.93‰ and 13.3 ± 8.4‰). Variation amplitudes (i.e., maximums − minimums) of the water vapor δ^2H, $\delta^{18}O$, and *d-excess* were 153.8‰, 27.69‰, and 82.5‰ in 2019, and were 124.5‰, 20.78‰, and 77.7‰ in 2020. The δ^2H and $\delta^{18}O$ of atmospheric water vapor gradually decreased with the vertical measurement heights from 1 m to 3 m and 15 m in both 2019 and 2020. In contrast, the *d-excess* of water vapor increased from the lower (1 m) to the upper (15 m) canopy during the two years of study periods. The difference in atmospheric water vapor δ^2H, $\delta^{18}O$, and *d-excess* was only significant between 1 m and 15 m ($P < 0.05$) in 2019. The isotopic values of atmospheric water vapor changed drastically between 1 m and 15 m ($P < 0.001$) in 2020; and the atmospheric water vapor $\delta^{18}O$ and *d-excess* differed significantly between 1 m and 3 m ($P < 0.001$) in 2020.

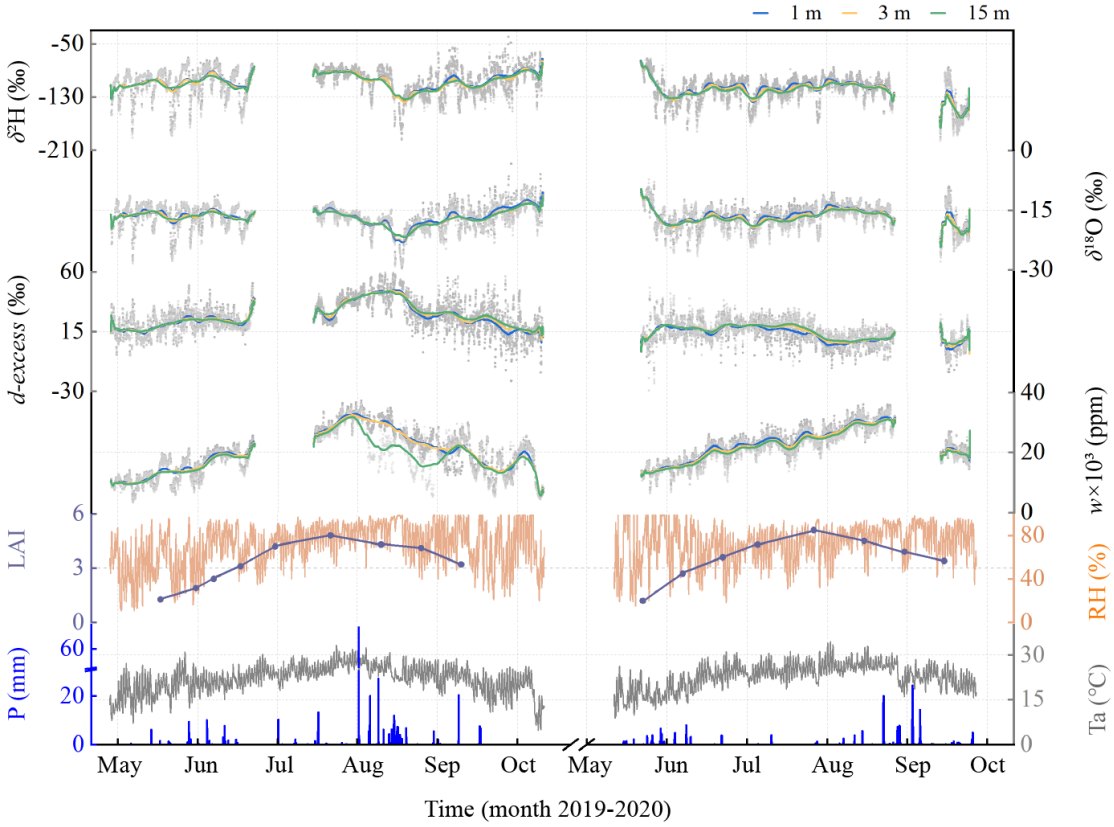

Figure 2. Time series of hourly atmospheric water vapor δ^2H, δ^{18}O, and *d-excess*, water vapor concentration (*w*), leaf area index (LAI), relative humidity (RH), precipitation (P), and surface air temperature (T_a) during the 2019-2020 growing (May-September) seasons. The Gaussian smoothing curves are shown for the in-situ atmospheric water vapor measurements at heights of 1 m (blue lines), 3 m (yellow lines), and 15 m (green lines).

The *w* of atmospheric water vapor was highest in August with single-peaked curves of seasonal variations (Figure 2). However, the peak of water vapor *w* in 2019 (36959.8 ppm) was delayed for 25 days compared to the peak (36090.8 ppm) in 2020. Furthermore, there were apparent differences in the atmospheric water vapor *w* between 1 m (or 3 m) and 15 m in 2019 ($P < 0.001$). During the growing (May-September) seasons, the LAI of reeds were 3.3 ± 1.2 in 2019 and 3.6 ± 1.2 in 2020. The mean RH in 2019 and 2020 were 70.7 ± 19.7 and 72.6 ± 17.5, respectively. The total rainfall was 37.6% lower in 2020 (414.1 mm) compared to 2019 (663.8 mm), indicating a weak summer monsoon year in 2020. The T_a of the experimental station was relatively constant with mean values of 21.9 ± 4.7 °C in 2019 and 22.8 ± 4.3 °C in 2020 during the study periods.

Table 1 Monthly average values of Water Vapor Concentration (*w*), Leaf Area Index (LAI), Relative Humidity (RH), Total Precipitation (P), Surface Air Temperature (T_a), and Isotopic Values of Atmospheric Water Vapor (δ^2H, δ^{18}O, and *d-excess*) in Liaodong Bay, China, from May-September 2019 and 2020

Month	*w* (ppm)[a]	LAI ($m^2\ m^{-2}$)	RH (%)	P (mm)	T_a (°C)	δ^2H (‰)			δ^{18}O (‰)			*d-excess* (‰)		
						1 m	3 m	15 m	1 m	3 m	15 m	1 m	3 m	15 m
May	12045.5	1.6	54.1	66.1	18.3	−111.1	−111.8	−112.5	−16.31	−16.40	−16.49	19.4	19.4	19.4
Jun	18875.6	3.3	69.4	44.9	22.0	−104.4	−105.8	−107.2	−16.10	−16.25	−16.31	24.4	24.2	23.3
Jul	29870.6	4.4	78.	55.8	25.6	− 97.2	−97.5	−98.3	−12.79	−12.88	−13.00	33.7	34.1	34.2
Aug	25471.5	4.0	82.6	424.1	24.9	−113.2	−114.3	−115.0	−18.54	−18.77	−18.87	35.2	35.8	35.9
Sep	18040.9	3.2	70.1	107.9	26.0	−102.6	−104.9	−104.5	−15.47	−15.91	−16.02	21.2	22.2	23.4
May	14714.6	1.8	70.2	85.9	16.7	−117.9	−118.8	−119.2	−16.75	−16.93	−16.96	15.9	16.4	16.3
Jun	20746.6	3.4	64.6	29.2	23.1	−118.3	−120.3	−122.4	−16.99	−17.34	−17.61	17.6	18.4	18.6
Jul	25200.8	4.5	70.7	11.5	25.4	−113.1	−114.8	−116.3	−15.60	−16.03	−16.34	11.7	13.3	14.6
Aug	30488.3	4.2	80.6	253	25.5	−115.0	−115.7	−116.7	−15.46	−15.60	−15.76	8.6	9.0	9.4
Sep	20180.2	3.3	77.6	34.8	21.7	−144.3	−146.1	−148.7	−18.73	−19.09	−19.54	5.6	6.6	7.6

[a] The monthly w of atmospheric water vapor was calculated based on the average of data from the lower (1 m), middle (3 m), and upper (15 m) canopy.

3.2 Long time scale variations

Figure 3 presents the diurnal variations of atmospheric water vapor δ^2H, δ^{18}O, and *d-excess* measured at heights of 1 m, 3 m, and 15 m. A clear diurnal cycle of water vapor δ^2H, δ^{18}O, and *d-excess* existed in both 2019 and 2020. The atmospheric water vapor δ^2H and δ^{18}O generally increased from 9:00 (LST) to 18:00 (LST). Simultaneously, the δ^2H and δ^{18}O of water vapor progressively declined to their minimum around 8:00-9:00 (LST) on the next day (Figure 3a-d). The diurnal variations of atmospheric water vapor δ^2H and δ^{18}O were less pronounced in 2020 than in 2019. Nonetheless, the diurnal variations of atmospheric water vapor *d-excess* were pretty clear in both years of 2019 and 2020, which had an opposite diurnal trend to that of atmospheric water vapor δ^2H and δ^{18}O (Figure 3e-f). The isotopic differences of atmospheric water vapor across measurement heights (i.e., 1, 3, and 15 m) were more evident in the daytime (8:00-20:00 LST) than at night (20:00-8:00 LST). This phenomenon appeared extremely typical in 2020, during which the atmosphere water vapor δ^2H and δ^{18}O declined progressively with the increase of heights ($P < 0.05$).

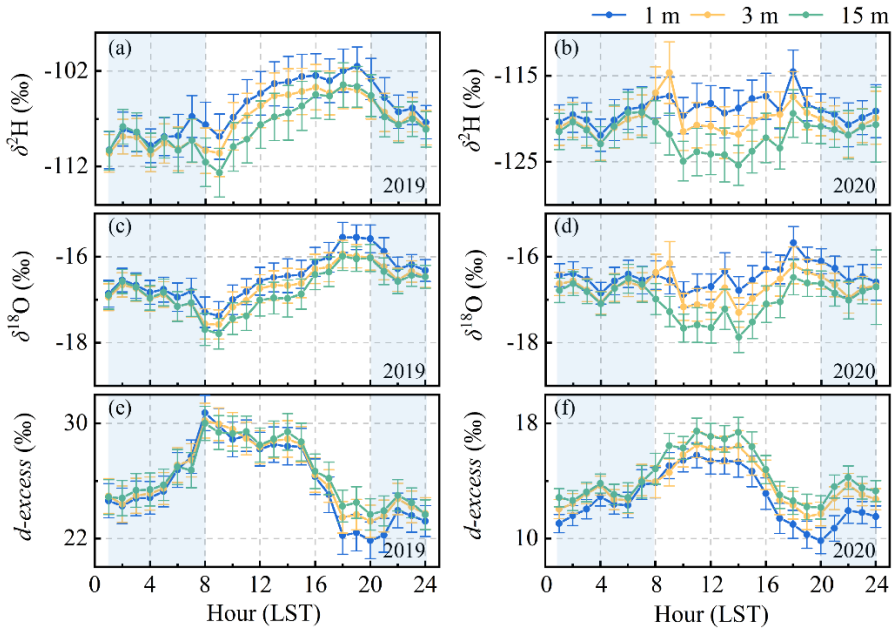

Figure 3. Twenty-four-hour variations of atmospheric water vapor δ^2H (**a**, **b**), δ^{18}O (**c**, **d**), and *d-excess* (**e**, **f**) measured at heights of 1 m (blue lines), 3 m (yellow lines), and 15 m (green lines) during the 2019-2020 growing (May-September) seasons. Error bars represent standard errors of the isotopic data in every hour. Shadow areas indicate the periods of time at night (20:00-8:00 LST).

Figure 4 illustrates the impacts of rainfall processes on the diurnal cycles of atmospheric water vapor δ^2H, δ^{18}O, and *d-excess* at 15 m height. Six rainfall events of different rainfall amounts (P = 2.6-141.1 mm) were selected during the 2019-2020 growing (May-September) seasons. The duration (D) of these rainfall events ranged from 11 h to 100 h. The δ^2H, δ^{18}O, and *d-excess* of atmospheric water vapor increased slightly after two small rainfall events (P = 2.6-4.5 mm, in Figure 4a-b). The peak-to-peak variations of atmospheric water vapor δ^2H, δ^{18}O, and *d-excess* were 31.8-51.6‰, 3.08-7.02‰, and 12.7-26.2‰, respectively. With the increase in

intensity and duration of rainfall, the isotopic values of atmospheric water vapor also increased during the rainfall processes (Figure 4c-d). However, the isotopic values of atmospheric water vapor declined after a 20 h continuous rainfall event. The variability of atmospheric water vapor in these moderate rainfall events (P = 30.9-33.4 mm) increased to 68.4-70.8‰ for δ^2H, 7.15-8.87‰ for δ^{18}O, and 20.3-34.3‰ for *d-excess*. The δ^2H, δ^{18}O, and *d-excess* of atmospheric water vapor decreased drastically during the heavy rainfall events as expected (Figure 4e-f). The isotopic variations of atmospheric water vapor in heavy rainfall events (P = 68.4-141.1 mm) were 37.4-66.8‰ for δ^2H, 3.41-5.70‰ for δ^{18}O, and 22.5-26.8‰ for *d-excess*.

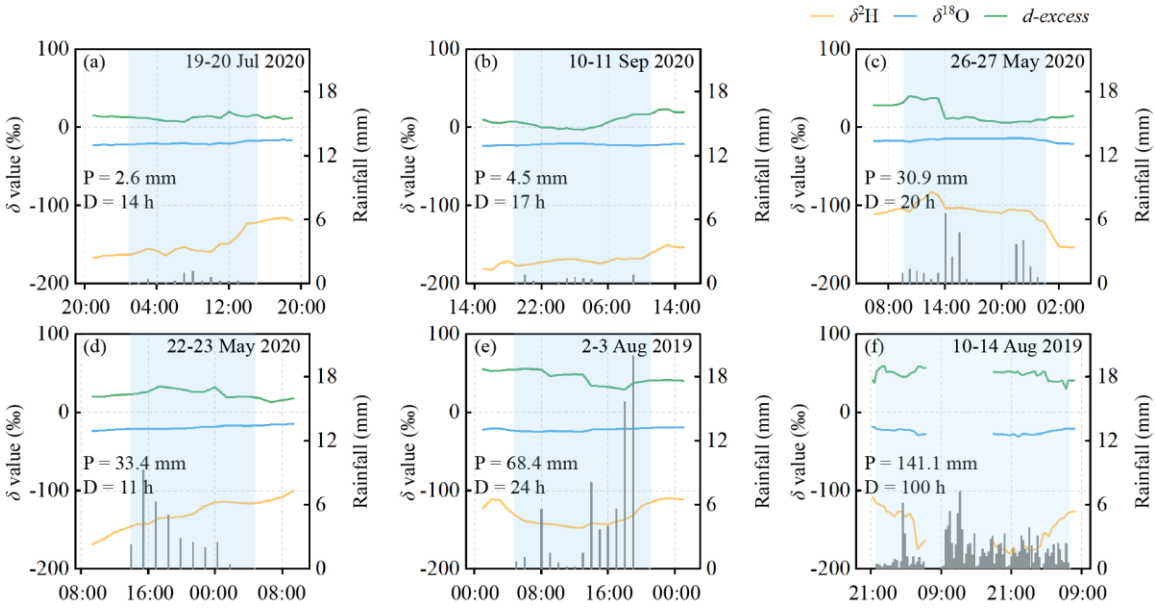

Figure 4. Impacts of rainfall processes on the diurnal cycles of atmospheric water vapor δ^2H, δ^{18}O, and *d-excess* at 15 m height (**a-f**) during the (2019-2020) study periods. Rainfall amount (P) and rainfall duration (D) are plotted on each panel for reference. Shadow areas indicate the periods of rainfall events.

3.3 Relationships with meteorological variables

Figure 5 depicts the linear dependency of δ^2H on δ^{18}O for atmospheric water vapor during the 2019-2020 growing (May-September) seasons. The hourly measurement of three (i.e., 1 m, 3 m, and 15 m) canopy layers were merged to reflect the impacts of rainfall events on the co-variations between δ^2H on δ^{18}O of atmospheric water vapor. This treatment was adopted due to the similar functions among different heights (*SI Appendix A*, Figure S1). In 2019, the δ^2H and δ^{18}O of atmospheric water vapor mainly occupied the dual-isotope plots from the global meteoric water line (GMWL: $\delta^2H = 8 \times \delta^{18}O + 10$) to its left sides (Figure 5a). Slopes of the atmospheric water vapor lines in 2019 were 6.4 ± 0.2 (R^2 = 0.87, P < 0.001) and 6.2 ± 0.1 (R^2 = 0.76, P < 0.001) during the rainfall and non-rainfall periods, respectively. In 2020, the δ^2H and δ^{18}O of atmospheric water vapor were plotted right on the GMWL (Figure 5b). Slopes of the atmospheric water vapor lines in 2020 were 7.4 ± 0.2 (R^2 = 0.89, P < 0.001) and 6.4 ± 0.1 (R^2 = 0.87, P < 0.001) during the rainfall and non-rainfall periods, respectively. The intercepts of the atmospheric water vapor lines were less than 10 for both years, ranging from 2.8 to 4.5 during the rainfall periods, and from – 13.8 to – 3.8 during the non-rainfall periods.

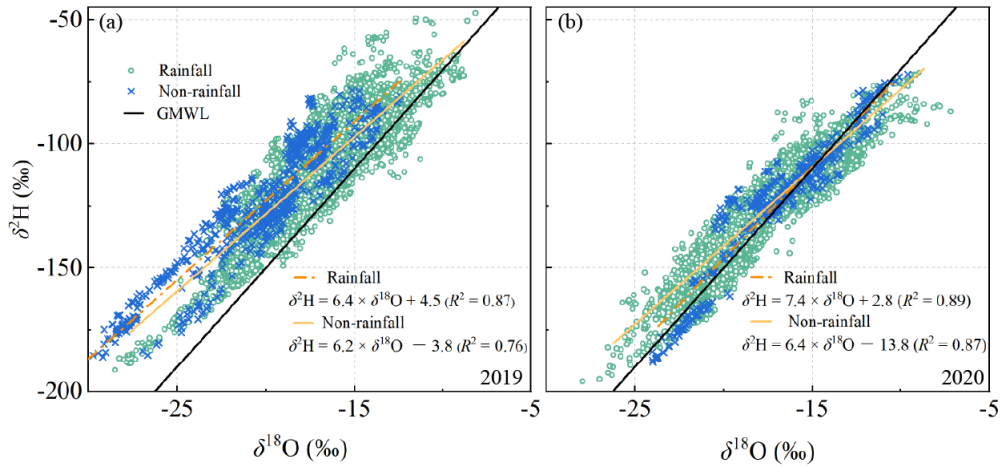

Figure 5. Isotopic values of δ^2H as a function of δ^{18}O in atmospheric water vapor during the 2019 (**a**) and 2020 (**b**) growing (May-September) seasons. Data of atmospheric water vapor δ^2H and δ^{18}O are divided into two groups representing the periods with rainfall and non-rainfall events. The global meteoric water line (GMWL: $\delta^2H = 8 \times \delta^{18}O + 10$) is also plotted on each panel for reference.

Figure 6 shows the relationships between the δ^2H, δ^{18}O and *d-excess* of atmospheric water vapor and local meteorological factors. The δ^2H and δ^{18}O of atmospheric water vapor were positively correlated with the water vapor concentration (*w*) (Figure 6a, 6d, 6g, and 6j). In contrast, their *d-excess* were negatively correlated with *w* in 2019 (R^2 = 0.05, $P < 0.001$, measurement undertaken at height of 15 m, in Figure 6m) and 2020 (R^2 = 0.11-0.16, $P < 0.001$, in Figure 6p). The atmospheric water vapor δ^2H, δ^{18}O and *d-excess* were weakly dependent on the relative humidity (RH) during the study periods (R^2 = 0.01-0.11, $P < 0.001$, in Figure 6b, 6e, 6h, 6k, 6n, and 6q). The δ^2H, δ^{18}O of atmospheric water vapor exhibited positive dependences on surface air temperature (T_a) in 2020 (R^2 = 0.05-0.07, P < 0.001, in Figure 6f and 6l). The atmospheric water vapor d-excess in 2020 was negatively correlated with T_a (R^2 = 0.01-0.02, $P <$ 0.001, in Figure 6r). However, no significant correlation occurred between the atmospheric water vapor isotopes and T_a in 2019 (Figure 6c, 6i, and 6o).

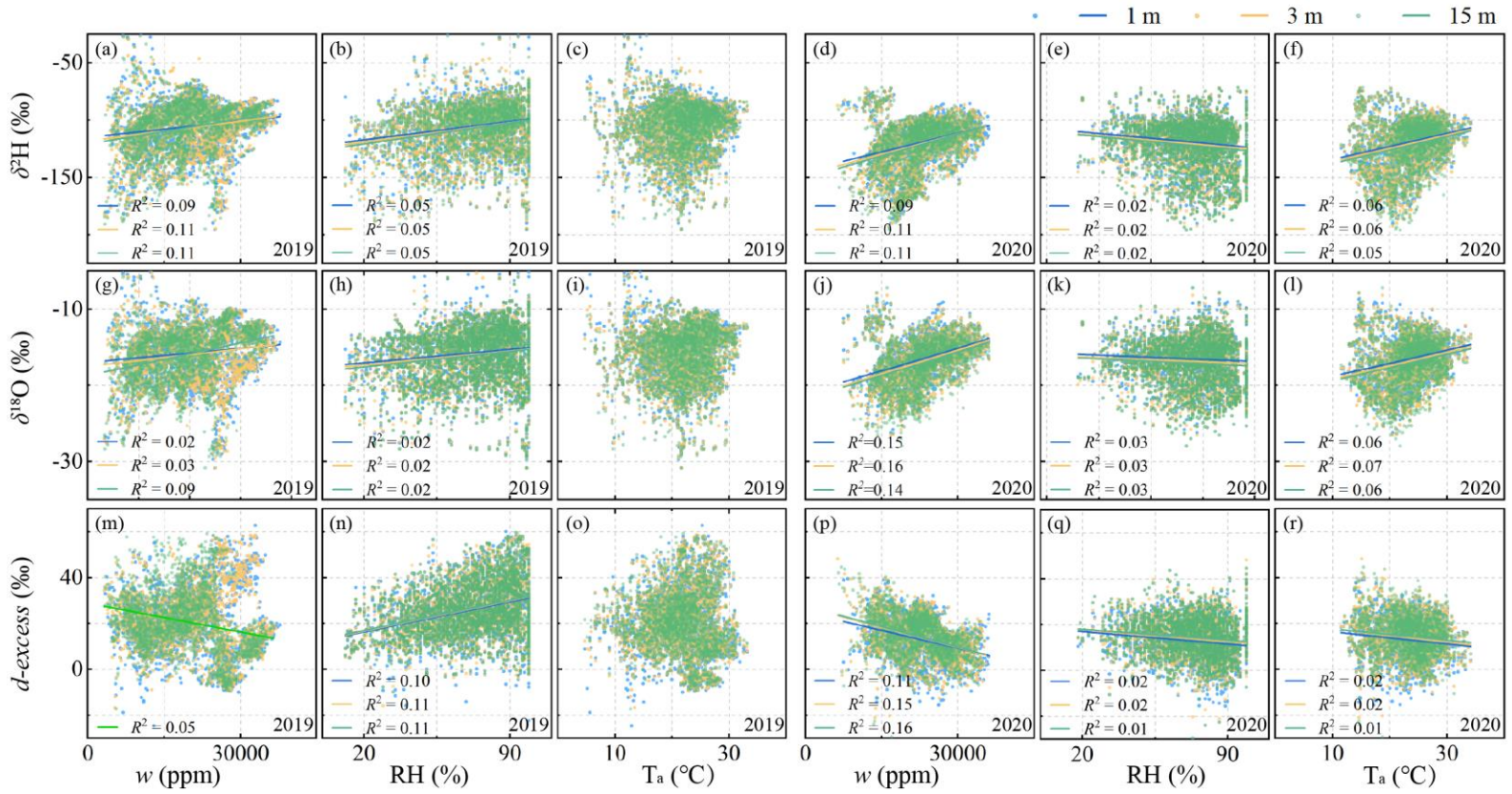

Figure 6. Correlations of the water vapor concentration (*w*), relative humidity (RH), and surface air temperature (T_a) with the atmospheric water vapor δ^2H (**a-f**), δ^{18}O (**g-l**), and *d-excess* (**m-r**) during the (2019-2020) study periods. The regression curves represent the in-situ atmospheric water vapor measurements at heights of 1 m (blue lines), 3 m (yellow lines), and 15 m (green lines).

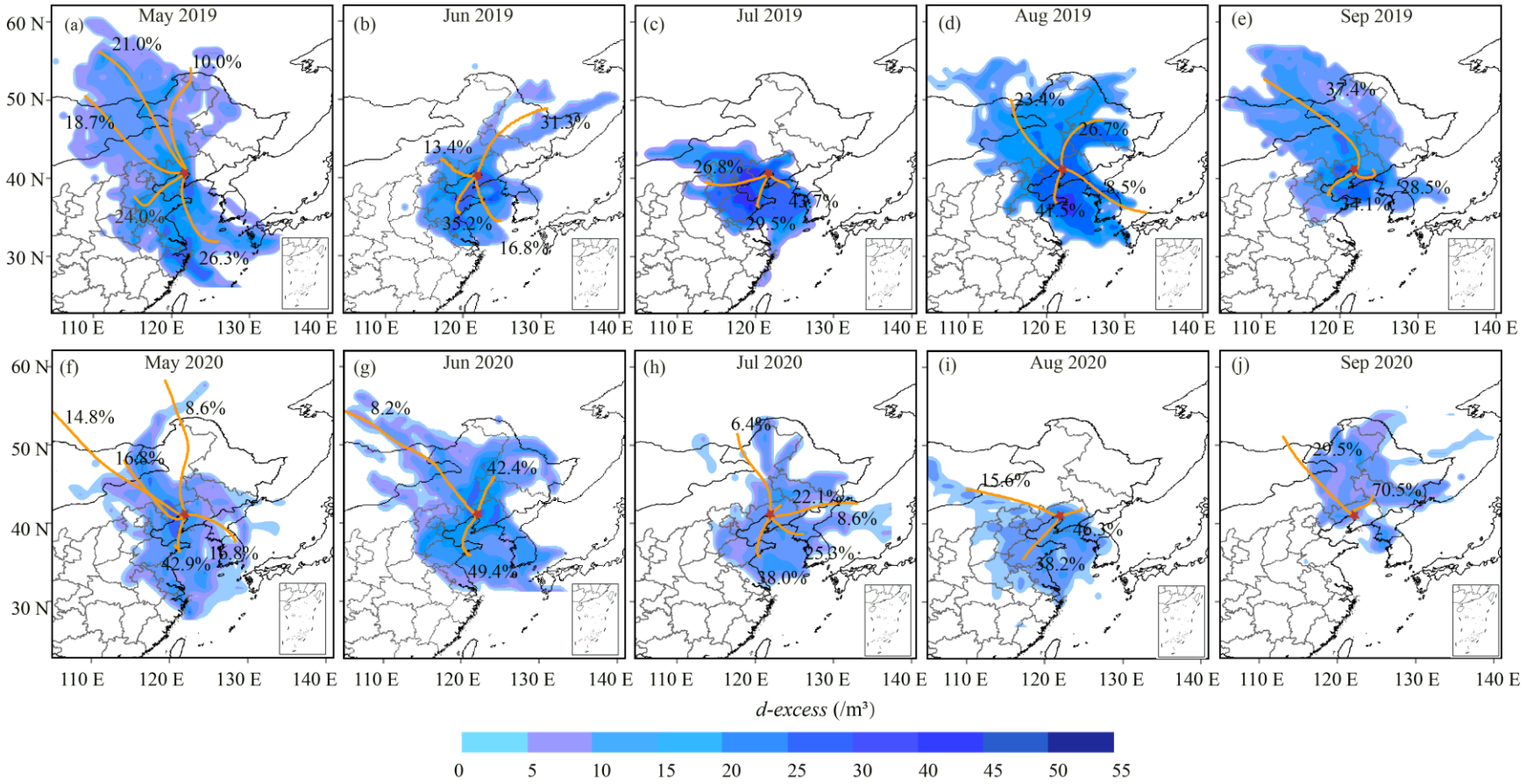

Figure 7. Back trajectory frequencies clustered according to the directions of air masses and the concentration fields of atmospheric water vapor *d-excess* during the 2019 (**a-e**) and 2020 (**f-j**) growing (May-September) seasons. Red star indicates the location of Panjin experimental station. Orange lines are the clusters of air masses during the preceding 48 h at 500 m height above the ground, and blue shading is the potential source of atmospheric water vapor *d-excess* in each month.

3.4 Large scale atmosphere circulations

Figure 7 shows the concentration fields of atmospheric water vapor *d-excess* along the backward trajectories at Panjin experimental station. The 48-hourly backward trajectories of air masses were calculated for the 2019-2020 growing (May-September) seasons. For all five months, 3659 and 3515 trajectories were clustered in 2019 and 2020, respectively (*SI Appendix A*, Figure *S2*). Then, we identified three-five major moisture source sectors that affected the experimental station. The dominant air masses in this region generally came from ocean sources, contributing more than 50% to the total air moisture except in June 2020 (49.4%). The transport paths of ocean air masses could be further clustered into two sectors, i.e., Southwest-South (SW-S) and South-Southeast (S-SE) directions. At the beginning of the monsoon season (May-June), the trajectory paths of air masses usually originated from ocean surfaces and the northern interior (Figure 7a-b and 7f-g). The ocean air masses gradually dominated during the peak monsoon season (July-August). The contribution proportions of ocean air masses reached the maxima in July 2019 (73.2%, in Figure 7c) and in August 2020 (84.5%, in Figure 7i). The influence of summer monsoon on local air masses weakened in September 2019, with a contribution proportion of 59.9% (Figure 7e). However, the ocean air masses had a prolonged impact (70.5%) on atmospheric water vapor *d-excess* at the experimental station in September 2020 (Figure 7j).

The back-air mass trajectory analysis indicates that seasonal dynamic in moisture sources was a main driving factor of the atmospheric water vapor *d-excess* variability (Figure 7). The spatial distribution of atmospheric water vapor *d-excess* at this experimental station was closely linked with the monsoon activities in East Asia. Most of trajectory paths were accompanied by relatively higher atmospheric water vapor *d-excess* in 2019 than in 2020. This phenomenon was particularly evident in 2019 (Figure 7a-e), where high-value of atmospheric water vapor *d-excess* commonly distributed around the coastal regions. Lower proportion of air masses arose from the ocean sources between August and September in 2019 (50-59.9%, in Figure 7d-e) than in 2020 (70.5-84.5%, in Figure 7i-j). However, the intensity of the East Asian monsoon was weak in 2020, which brought less rainfall to the atmospheric water cycles in Liaodong Bay. Therefore, the air masses from the interiors of North China had more significant impacts (i.e., more negative values) on the atmospheric water vapor *d-excess* in 2020 than in 2019. The secondary moisture sources of inland air masses played a vital role in the seasonal variations of atmospheric water vapor *d-excess* in the weak summer monsoon year.

4 Discussion

Based on the in-situ measurement techniques, this study revealed the isotopic signatures of atmospheric water vapor (Figure 2-4), as well as the driving forces of the atmospheric water vapor isotopes (Figure 5-7) for a reed wetland of Liaodong Bay, Northeast China. The meteorological factors (e.g., water vapor concentration, relative humidity, and air temperature) were incapable of predicting the variations of atmospheric water vapor $\delta^{2}H$, $\delta^{18}O$, and *d-excess* in this region. The different seasonal and diurnal patterns of water vapor isotopes could be attributed to the stronger monsoon activities in 2019 than in 2020. These findings would broaden our understanding of hydrological cycles in the coastal wetlands.

4.1 Temporal dynamics of water vapor isotopes at different heights

The long- (i.e., seasonal scale) and short- (i.e., diurnal scale) term characteristics of atmospheric water vapor isotopes showed significant variations at heights of 1 m, 3 m, and 15 m (Figure 2 and 3). The temporal dynamics of water vapor δ^2H, δ^{18}O, and *d-excess* are usually controlled by the atmospheric processes (Lee et al., 2005; Wen et al., 2008), local evapotranspiration (Aron et al., 2019; Huang & Wen, 2014), and synoptic events (Berkelhammer et al., 2013; Wu et al., 2019). For instance, Steen-Larsen et al. (2013) suggested that the intra-seasonal variations of water vapor isotopes mainly result from the interplay between large-scale moisture advection, boundary layer dynamics, and local moisture fluxes above the Greenland Ice Sheet. The magnitude of changes in surface water vapor *d-excess* can be as high as 40‰ or greater during several episodes (Steen-Larsen et al., 2013). Huang & Wen (2014) reported that the atmospheric water vapor δ^2H, δ^{18}O, and *d-excess* are dominated by the typical arid and continental climates, which will not show clear seasonal cycles in the inland region of Northwest China. As a typical coastal wetland under the influence of the East Asian Monsoon, our results showed that the temporal patterns of water vapor isotopes were strikingly different between the years of study periods. Moreover, some departures of atmospheric water vapor isotopes were observed among the three measurement heights. This might be interpreted as the enrichment effects of local evapotranspiration, which gradually improves the atmospheric water vapor isotopes with the increasing plant physiological activities (Hu et al., 2021; Welp et al., 2012).

The seasonal variations of atmospheric water vapor δ^2H, δ^{18}O, and *d-excess* in the reed wetlands of Liaodong Bay were different from those of the other research site (Fiorella et al., 2018; Laonamsai et al., 2021; Lee et al., 2006; Wen et al., 2010). Apart from the noticeable seasonal changes occurring in each year, there were distinct inter-annual cycles for atmospheric water vapor isotopes between 2019 and 2020 (Figure 2). The mean isotopic values of atmospheric water vapor ranged from − 120.7‰ to − 108.4‰ for δ^2H, from − 16.98‰ to − 16.64‰ for δ^{18}O, and from 13.3‰ to 26.3‰ (Table 1), which were higher than the results reported by Wen et al. (2010) and Zhang et al. (2011) in inland areas of China. Especially in 2019, the δ^2H and δ^{18}O of atmospheric water vapor fluctuated seasonally with lower values in the prevailing monsoon season (i.e., August-September). The seasonal pattern of atmospheric water vapor δ^2H and δ^{18}O made a complete reversal of the water vapor concentration (*w*) trend (Figure 2). In fact, the summer monsoon was earlier in 2019 and brought more rainfall than in 2020. In 2019, the typhoon "Lekima" was reported to land in Southwest coast of China (4-10 August) with a wind speed of 51.4 m s^{-1}, which then moved northwards and made a second landfall in Liaodong Bay (Wang et al., 2021). Some studies reported that a significant decrease in precipitation and atmospheric isotopes can happen during the tropical typhoons (Bonne et al., 2019; Conroy et al., 2016). The abrupt decline of atmospheric water vapor *w* at 15 m height could also be attributed to the high condensation efficiency and strong entrainment activity during the typhoon event in 2019.

The interactions between atmospheric entrainment and local evapotranspiration typically dominate the diurnal cycles of atmospheric water vapor δ^2H, δ^{18}O, and *d-excess* (Aron et al., 2019; Huang & Wen, 2014; Lee et al., 2007; Zhao et al., 2014). Our results showed that the δ^2H and δ^{18}O of atmosphere were lower in the early morning (8:00-9:00 LST) than in the late afternoon (16:00-18:00 LST). On the contrary, the atmospheric water vapor *d-excess* exhibited an "inverted U-shaped diurnal pattern" in 2019 and 2020 (Figure 3). The downward trends in atmospheric water vapor δ^2H and δ^{18}O can be attributed to the rapid increase of free air in ABL

514 when plant transpiration activity is relatively low in the morning (Huang & Wen, 2014). The
515 enrichment roles of local evapotranspiration surpassed the depletion effects of atmospheric
516 entrainment in the late afternoon. Such positive impacts of local evapotranspiration on
517 atmosphere isotopes were marked significantly in the lower (1 m) canopy than in the middle (3
518 m) and upper (15 m) heights (Figure 3). Apparently, the rainfall process was one of the main
519 factors contributing to the diurnal dynamics of atmospheric water vapor δ^2H, δ^{18}O, and *d-excess*
520 (Figure 4). The isotopic fractionation caused by the sub-cloud secondary evaporation enriches
521 the residual rainfall, which in turn can make the enrichment of atmospheric isotopes during small
522 rainfall events (Vuille et al., 2003; Wu et al., 2021). However, the rainout effects of rainfall
523 would result in the continuous depletion of atmospheric isotopes according to the Rayleigh
524 distillation mechanisms (Gat, 1996; Lee et al., 2005; Wen et al., 2010).

525 4.2 Controlling factors of water vapor isotopes above coastal wetlands

526 The global meteoric water line (GMWL: $\delta^2H = 8 \times \delta^{18}O + 10$) indicates the isotopic co-
527 variations in marine water that has not been exposed to evaporation fractionation (Craig, 1961;
528 Gat, 1996). As the marine air masses move over the coastal regions and towards the inland, the
529 air parcels will be mixed with continental water vapor sources and influenced by geographic
530 parameters such as the distances from coasts, altitudes, rainfall processes, and temperatures
531 (Christner et al., 2018; Gat, 1996; Merlivat & Jouzel, 1979). The slopes of atmospheric water
532 vapor lines (6.2-7.4) were lower than that of GMWL (Figure 5), which were determined by the
533 non-equilibrium fractionation (i.e., the existence of kinetic effects) within air parcels. Similarly,
534 Bastrikov et al. (2014) reported that the overall slopes of atmospheric water vapor lines are 5.6-
535 7.7 among different seasons in western Siberia (Kourovka). Li et al. (2020) highlighted that the
536 slopes of atmospheric water vapor lines change from 7.0 to 7.6 during a six-year period in
537 Eastern China. The high intercept (i.e., *d-excess*) of atmospheric water vapor lines in 2019
538 suggested that the isotopic changes in air masses which were very sensitive to the moisture
539 source conditions (Aemisegger et al., 2014; Delattre et al., 2015; Fiorella et al., 2018).

540 The results of this study also showed that the relationships between local meteorological
541 factors and atmospheric water vapor isotopes were weak or nonexistent at Panjin experimental
542 station (Figure 6). This finding was inconsistent with previous observations in the inland areas of
543 China. For example, Zhang et al. (2011) noted that the water vapor concentration (*w*) can be an
544 excellent predictor of atmospheric water vapor δ^2H, δ^{18}O, and *d-excess* based on the Rayleigh
545 distillation. However, the weak correlations between atmospheric water vapor isotopes and
546 relative humidity (RH) were found in other studies (Li et al., 2020; Salamalikis et al., 2015). An
547 earlier study by Lee et al. (2006) in New England found that the atmospheric w is a better
548 indicator for atmospheric water vapor isotopes than air temperature (T_a) on short time scales.
549 These studies have established a certain level of correlation between atmospheric water vapor
550 isotopes and local meteorological factors (e.g., *w*, T_a, and RH) during the non-monsoon season
551 (Lee et al., 2005; Li et al., 2020; Noone et al., 2012). In contrast, Wen et al. (2010) found that the
552 *w* becomes a poor predictor of the atmospheric water vapor δ^2H, δ^{18}O, and *d-excess* during the
553 summer monsoon season. Similar to this study, weak correlations were also found by Li et al.
554 (2020) and Wang et al. (2021) during the peak monsoon activities.

555 Unlike the δ^2H and δ^{18}O whose temporal variations are commonly overwhelmed by the
556 Rayleigh distillation and/or the rainout history of air masses, the atmospheric water vapor *d-*
557 *excess* of an air mass is a nearly constant tracer during the transport processes (Welp et al., 2012;

Wei et al., 2019). Therefore, the *d-excess* of atmospheric water vapor is widely used as a conservative indicator for identifying the moisture source locations (Aemisegger et al., 2014; Steen-Larsen et al., 2015; Uemura et al., 2008; Xu et al., 2022). Panjin experimental station was situated on the special borderland between the North China Plain and Bohai Sea (Figure 1), which was also located within the edge of the East Asian monsoon region (Luo et al., 2021; Wang et al., 2021). With the sea in three directions, the atmospheric water vapor *d-excess* in this study was significantly affected by the ocean air masses (Figure 7). The high values of atmospheric water vapor *d-excess* consistently appeared in the peak (i.e., July-August) monsoon season. The results of the present study further confirmed that the ocean air masses dominated the temporal variations of atmospheric water vapor *d-excess* (Figures 2, 3, and 7) when a super typhoon "Lekima" happened in 2019 (details in Section 4.1). Lai et al. (2018) examined the atmospheric water cycling above a coastal mangrove forest in Southern China. They also found that the substantial increase of atmospheric water vapor *d-excess* is related to the passage of a tropical typhoon "Talas" (Lai et al., 2018). In the Qinghai-Tibetan Plateau of central Asia, Wu et al. (2019) revealed that high *d-excess* values of atmospheric water vapor were influenced by local moisture mixing during the monsoon season. A recent study noted that high values of atmospheric water vapor *d-excess* appear before the monsoon onset and after the monsoon season at Lhasa in Southern Tibetan Plateau (Tian et al., 2020). Indeed, air masses from cold and dry areas can also bring a relatively high atmospheric water vapor *d-excess* (Uemura et al., 2008; Xu et al., 2022). Further mechanism studies are expected to provide more rational explanations for the above-mentioned processes in coastal wetlands.

5 Conclusions

The inter-annual variations of atmospheric water vapor δ^2H, δ^{18}O, and *d-excess* were significantly different between 2019 and 2020. On a seasonal time scale, the mean isotopic values of atmospheric water vapor in 2019 were significantly higher than that in 2020. Meanwhile, the δ^2H and δ^{18}O of atmospheric water vapor gradually decreased from the lower (1 m), to the middle (3 m) and upper (15 m) canopy both 2019 and 2020. A clear diurnal cycle of atmospheric water vapor isotopes existed during the study periods, which was more pronounced in 2019 than in 2020. The diurnal isotopic differences of atmospheric water vapor among measurement heights (i.e., 1, 3, and 15 m) were more evident in the daytime (8:00-20:00 LST) than at night (20:00-8:00 LST). Rainfall events had a significant impact on the diurnal dynamics of atmospheric water vapor δ^2H, δ^{18}O, and *d-excess*, depending on the rainfall intensity (i.e., amount and duration). The correlations between atmospheric water vapor isotopes and local meteorological factors were weak or nonexistent in the study region. Instead, the spatial-temporal dynamics of atmospheric water vapor isotopes were highly consistent with the monsoon activities. The moisture in air masses could be clustered into three to-five primary sources, with over 60% from the ocean sources. High *d-excess* values reflected the predominating influences of ocean air masses on atmospheric water vapor cycles in the coastal regions.

Acknowledgments

We are deeply thankful to Ye Zhang, Long Chen, Xian-zhe Liu, and Han Wang (Panjin National Climatic Observatory, Institute of Atmospheric Environment, China Meteorological Administration) for field support. We would like to extend our thanks to Institutional Center for Shared Technologies and Facilities of Xishuangbanna Tropical Botanical Garden, Chinese Academy of Sciences for laboratory process support. We also acknowledge the NOAA-Air Resources Laboratory (ARL) for providing the HYSPLIT model and meteorological data. This research was supported by the National Natural Science Foundation of China [32171557, 32171529], the Yunnan Natural Science Foundation [202201AT070221], the Youth Innovation Promotion Association of Chinese Academy of Sciences [2021397], the National Science and Technology Basic Resources Survey Program of China [2019FY0101302], the National Key R&D Program of China [2022YFF0801301], the Key Project of Liaoning Provincial Meteorological Bureau [LNCP202205].

Open Research

Data for this study consist of water isotopes and environmental variables that are available at https://doi.org/10.11888/Atmos.tpdc.272899

References

Aemisegger, F., Pfahl, S., Sodemann, H., Lehner, I., Seneviratne, S. I., & Wernli, H. (2014). Deuterium excess as a proxy for continental moisture recycling and plant transpiration. *Atmospheric Chemistry and Physics*, *14*(8), 4029-4054. https://doi.org/10.5194/acp-14-4029-2014

Araguas-Araguas, L., Froehlich, K., Rozanski, K. (2000). Deuterium and oxygen-18 isotope composition of precipitation and atmospheric moisture. *Hydrological Processes, 14*(8), 1341-1355. https://doi.org/10.1002/1099-1085(20000615)14:8<1341::Aid-hyp983>3.0.Co;2-z

Aron, P. G., Poulsen, C.J., Fiorella, R. P., & Matheny, A. M. (2019). Stable water isotopes reveal effects of intermediate disturbance and canopy structure on forest water cycling. *Journal of Geophysical Research: Biogeosciences*, *124*(10), 2958-2975. https://doi.org/10.1029/2019jg005118

Bagheri, R., Bagheri, F., Karami, G. H., & Jafari, H. (2019). Chemo-isotopes (^{18}O & ^{2}H) signatures and HYSPLIT model application: Clues to the atmospheric moisture and air mass origins. *Atmospheric Environment, 215*, 116892. https://doi.org/10.1016/j.atmosenv.2019.116892

Bailey, A., Noone, D., Berkelhammer, M., Steen-Larsen, H. C., & Sato, P. (2015). The stability and calibration of water vapor isotope ratio measurements during long-term deployments. *Atmospheric Measurement Techniques*, 4521-4538. https://doi.org/10.5194/amt-8-4521-2015

Bastrikov, V., Steen-Larsen, H. C., Masson-Delmotte, V., Gribanov, K., Cattani, O., Jouzel, J., & Zakharov, V. (2014). Continuous measurements of atmospheric water vapour isotopes in

western Siberia (Kourovka). *Atmospheric Measurement Techniques*, *7*(6), 1763-1776. https://doi.org/10.5194/amt-7-1763-2014

Berkelhammer, M., Hu, J., Bailey, A., Noone, D. C., Still, C. J., Barnard, H., et al. (2013). The nocturnal water cycle in an open-canopy forest. *Journal of Geophysical Research: Atmospheres*, *118*(17), 10225-10242. https://doi.org/10.1002/jgrd.50701

Bonne, J. L., Behrens, M., Meyer, H., Kipfstuhl, S., Rabe, B., Schönicke, L., et al. (2019). Resolving the controls of water vapour isotopes in the Atlantic sector. *Nature Communications*, *10*(1), 1-10. https://doi.org/10.1038/s41467-019-09242-6

Bonne, J. L., Meyer, H., Behrens, M., Boike, J., Kipfstuhl, S., Rabe, B. et al. (2020). Moisture origin as a driver of temporal variabilities of the water vapour isotopic composition in the Lena River Delta, Siberia. *Atmospheric Chemistry and Physics*, *20*(17), 10493-10511. https://doi.org/10.5194/acp-20-10493-2020

Casado, M., Cauquoin, A., Masson-Delmotte, V., Genthon, C., Kerstel, E., Kassi, S., et al. (2016). Continuous measurements of isotopic composition of water vapour on the East Antarctic Plateau. *Atmospheric Chemistry and Physics*, *16*(13), 8521-8538. https://doi.org/10.5194/acp-16-8521-2016

Christner, E., Aemisegger, F., Pfahl, S., Werner, M., Cauquoin, A., Schneider, M. et al. (2018). The climatological impacts of continental surface evaporation, rainout, and subcloud processes on δD of water vapor and precipitation in Europe. *Journal of Geophysical Research: Atmospheres*, *123*(8), 4390-4409. https://doi.org/10.1002/2017jd027260

Christner, E., Kohler, M., & Schneider, M. (2017). The influence of snow sublimation and meltwater evaporation on δD of water vapor in the atmospheric boundary layer of central

662 Europe. *Atmospheric Chemistry and Physics*, *17*(2), 1207-1225.
663 https://doi.org/10.5194/acp-17-1207-2017
664 Conroy, J. L., Noone, D., Cobb, M. K., Moerman, J. W., & Konecky, B. L. (2016). Paired stable
665 isotopologues in precipitation and vapor: A case study of the amount effect within western
666 tropical Pacific storms. *Journal of Geophysical Research: Atmospheres*, *121*(7), 3290-3303.
667 https://doi.org/10.1002/2015jd023844
668 Craig, H. (1961). Isotopic variations in meteoric waters. *Science*, *133*(346), 1702-1703.
669 https://doi.org/10.1126/science.133.3465.1702
670 Cui, J. P., Tian, L. D., & Gibson, J. J. (2018). When to conduct an isotopic survey for lake water
671 balance evaluation in highly seasonal climates. *Hydrological Processes*, *32*(3), 379-387.
672 https://doi.org/10.1002/hyp.11420
673 Dahinden, F., Aemisegger, F., Wernli, H., Schneider, M. Diekmann, C.J., Ertl, B., et al. (2021).
674 Disentangling different moisture transport pathways over the eastern subtropical North
675 Atlantic using multi-platform isotope observations and high-resolution numerical
676 modelling. *Atmospheric Chemistry and Physics*, *21*(21), 16319-16347.
677 https://doi.org/10.5194/acp-21-16319-2021
678 Dansgaard W. (1964). Stable isotopes in precipitation. *Tellus*, *16*(4): 436-468.
679 https://doi.org/10.3402/tellusa.v16i4.8993
680 Delattre, H., Vallet-Coulomb C., & Sonzogni, C. (2015). Deuterium excess in the atmospheric
681 water vapour of a Mediterranean coastal wetland: regional vs. local signatures. *Atmospheric*
682 *Chemistry and Physics*, *15*(17), 10167-10181. https://doi.org/10.5194/acp-15-10167-2015

683 Devi, P., Jain, A. K., Rao, M. S., & Kumar B. (2014). Experimental study on isotope
684 fractionation of evaporating water of different initial isotopic composition. *Journal of*
685 *Radioanalytical and Nuclear Chemistry*, *302*(2), https://doi.org/10.1007/s10967-014-3368-7
686 Diekmann, C. J., Schneider, M., Knippertz, P., Vries, A. J., Pfahl, S., Aemisegger, F., et al.
687 (2021). A lagrangian perspective on stable water isotopes during the West African
688 Monsoon. *Journal of Geophysical Research: Atmospheres*, *126*(19), e2021JD034895.
689 https://doi.org/10.1029/2021jd034895
690 Farlin, J., Lai, C. T., & Yoshimura, K. (2013). Influence of synoptic weather events on the
691 isotopic composition of atmospheric moisture in a coastal city of the western United States.
692 *Water Resources Research*, *49*(6), 3685-3696. https://doi.org/10.1002/wrcr.20305
693 Fiorella, R. P., Poulsen, C. J. & Matheny, A. M. (2018). Seasonal patterns of water cycling in a
694 deep, continental mountain valley inferred from stable water vapor isotopes. *Journal of*
695 *Geophysical Research: Atmospheres*, *123*(14), 7271-7291.
696 https://doi.org/10.1029/2017jd028093
697 Fiorella, R. P., West, J. B., & Bowen, G. J. (2019). Biased estimates of the isotope ratios of
698 steady-state evaporation from the assumption of equilibrium between vapour and
699 precipitation. *Hydrological Processes*, *33*(19), 2576-2590.
700 https://doi.org/10.1002/hyp.13531
701 Galewsky, J., Jensen, M. P., & Delp, J. (2022). Marine boundary layer decoupling and the stable
702 isotopic composition of water vapor. *Journal of Geophysical Research: Atmospheres*,
703 *127*(3), e2021JD035470. https://doi.org/10.1029/2021jd035470

Galewsky, J., Rella, C., Sharp, Z., Samuels, K., & Ward, D. (2011). Surface measurements of upper tropospheric water vapor isotopic composition on the Chajnantor Plateau, Chile. *Geophysical Research Letters*, *38*(17), L17803. https://doi.org/10.1029/2011gl048557

Galewsky, J. Steen-Larsen, H. C., Field, R. D., Worden, J., Risi, C., & Schneider, M. (2016). Stable isotopes in atmospheric water vapor and applications to the hydrologic cycle. *Reviews of Geophysics*, *54*(4), 809-865. https://doi.org/10.1002/2015rg000512

Gat, J. R. (1996). Oxygen and hydrogen isotopes in the hydrologic cycle. *Annual Review of Earth and Planetary Sciences*, *24*, 225-262. https://doi.org/10.1146/annurev.earth.24.1.225

Gonzalez, Y., Schneider, M., Rodriguez, S., Christner, E., Garcia, O. E., Cuevas, E., et al. (2016). Detecting moisture transport pathways to the subtropical North Atlantic free troposphere using paired H_2O-δD in situ measurements. *Atmospheric Chemistry and Physics*, *16*(7), 4251-4269. https://doi.org/10.5194/acp-16-4251-2016

Griffis, T. J., Wood, J. D., Baker, J. M., Lee, X. H., Xiao, K., Chen, Z. C., et al. (2016). Investigating the source, transport, and isotope composition of water vapor in the planetary boundary layer. *Atmospheric Chemistry and Physics*, *16*(8), 5139-5157. https://doi.org/10.5194/acp-16-5139-2016

Hu, Y. B., Xiao, W., Wei, Z. W., Welp, L. R., Wen, X. F., & Lee, X. H. (2021). Determining the isotopic composition of surface water vapor flux from high-frequency observations using flux-gradient and keeling plot methods. *Earth and Space Science*, *8*(3), e2020EA001304. https://doi.org/10.1029/2020ea001304

Hu, Z. M., Wen, X. F., Sun, X. M., Li, L. H., Yu, G. R., Lee, X. H. & Li S. G. (2014). Partitioning of evapotranspiration through oxygen isotopic measurements of water pools

and fluxes in a temperate grassland. *Journal of Geophysical Research: Biogeosciences*, *119*(3), 358-371. https://doi.org/10.1002/2013jg002367

Huang, L. J., & Wen, X F. (2014). Temporal variations of atmospheric water vapor δD and δ^{18}O above an arid artificial oasis cropland in the Heihe River Basin. *Journal of Geophysical Research: Atmospheres*, *119*(19), 11456-11476. https://doi.org/10.1002/2014jd021891

Huang, Y. Y., Wang, B., Li, X. F., & Wang, H. J. (2018). Changes in the influence of the western Pacific subtropical high on Asian summer monsoon rainfall in the late 1990s. *Climate Dynamics*, *51*(1-2), 443-455. https://doi.org/10.1007/s00382-017-3933-1

Kurita, N., Newman, B. D., Araguas-Araguas, L. J., & Aggarwal, P. (2012). Evaluation of continuous water vapor δD and δ^{18}O measurements by off-axis integrated cavity output spectroscopy. *Atmospheric Measurement Techniques*, *5*(8), 2069-2080. https://doi.org/10.5194/amt-5-2069-2012

Lai, C.T., & Ehleringer, J. (2011). Deuterium excess reveals diurnal sources of water vapor in forest air. *Oecologia*, *165*(1), 213-223. https://doi.org/10.1007/s00442-010-1721-2

Lai, X., Wright, J. S., Huang, W. Y., Liang, J., Lin, G. H., & Zhu, S. X. (2018). Contributions of atmospheric transport and rain-vapor exchange to near-surface water vapor in the Zhanjiang Mangrove Reserve, southern China: an isotopic perspective. *Atmosphere*, *9*(9), 365. https://doi.org/10.3390/atmos9090365

Laonamsai, J., Ichiyanagi, K., Patsinghasanee, S., & Kamdee, K. (2021). Controls on stable isotopic characteristics of water vapour over Thailand. *Hydrological Processes*, *35*(7), e14202. https://doi.org/10.1002/hyp.14202

747 Lee, X. H, Sargent, S., Smith, R., & Tanner, B. (2005). In situ measurement of the water vapor
748 $^{18}O/^{16}O$ isotope ratio for atmospheric and ecological applications. *Journal of Atmospheric*
749 *and Oceanic Technology*, *22*(8), 1305-1305. https://doi.org/10.1175/JTECH9001.1a
750 Lee, X. H., Smith, R., & Williams, J. (2006). Water vapour $^{18}O/^{16}O$ isotope ratio in surface air in
751 New England, USA. *Tellus Series B-Chemical and Physical Meteorology*, *58*(4), 293-304.
752 https://doi.org/10.1111/j.1600-0889.2006.00191.x
753 Lee, X. H., Kim, K., & Smith R. (2007). Temporal variations of the $^{18}O/^{16}O$ signal of the whole-
754 canopy transpiration in a temperate forest. *Global Biogeochemical Cycles*, *21*, GB3013.
755 https://doi.org/10.1029/2006gb002871
756 Li, Y. J., An, W. L., Pang, H. X., Wu, S. Y., Tang, Y. Y., Zhang, W. B., & Hou, S.G. (2020).
757 Variations of stable isotopic composition in atmospheric water vapor and their controlling
758 factors-a 6-year continuous sampling study in Nanjing, eastern China. *Journal of*
759 *Geophysical Research: Atmospheres*, *125*, e2019JD031697.
760 https://doi.org/10.1029/2019jd031697
761 Luo, J. S., Sun, Y. H., Wang, Y. G., Xie, Z. H., & Meng, L. D. (2021). Cenozoic tectonic
762 evolution of the eastern Liaodong Bay sub-basin, Bohai Bay basin, eastern China-
763 Constraints from seismic data. *Marine and Petroleum Geology*, *134*, 105346.
764 https://doi.org/10.1016/j.marpetgeo.2021.105346
765 Mao, D.H., He, X.Y., Wang, Z.M., Tian, Y.L., Xiang, H.X., Yu, H., et al. (2019). Diverse
766 policies leading to contrasting impacts on land cover and ecosystem services in Northeast
767 China. Journal of Cleaner Production, *240*, 117961.
768 https://doi.org/10.1016/j.jclepro.2019.117961

769 Mao, D.H., Wang, Z.M., Du, B.J., Li, L., Tian, Y.L., Zeng, Y., et al. (2020). National wetland
770 mapping in China: A new product resulting from object based and hierarchical classification
771 of Landsat 8 OLI images. ISPRS Journal of Photogrammetry and Remote Sensing, 164, 11-
772 25 https://doi.org/10.1016/j.isprsjprs.2020.03.020
773 Mercer, J. J., Liefert, D. T., & Williams, D. G. (2020). Atmospheric vapour and precipitation are
774 not in isotopic equilibrium in a continental mountain environment. *Hydrological Processes*,
775 *34*(14), 3078-3101. https://doi.org/10.1002/hyp.13775
776 Merlivat, L., & Jouzel, J. (1979). Global climatic interperetation of the deuterium ^{18}O
777 relationship for precipitation. *Journal of Geophysical Research: Oceans*, *84*(C8), 5029-
778 5033. https://doi.org/10.1029/jc084ic08p05029
779 Munksgaard, N. C., Zwart, C., Haig, J., Cernusak, L. A., & Bird, M. I. (2020). Coupled rainfall
780 and water vapour stable isotope time series reveal tropical atmospheric processes on
781 multiple timescales. *Hydrological Processes*, *34*(1), 111-124.
782 https://doi.org/10.1002/hyp.13576
783 NFGA. (2010). National Wetland Survey Statistics Report. National Foresttry and Grassland
784 Administration (in Chinese). https://www.forestry.gov.cn
785 Noone, D. (2012). Pairing measurements of the water vapor isotope ratio with humidity to
786 deduce atmospheric moistening and dehydration in the tropical midtroposphere. *Journal of*
787 *Climate*, *25*(13), 4476-4494. https://doi.org/10.1175/jcli-d-11-00582.1
788 Parkes, S. D., McCabe, M. F., Griffiths, A. D., Wang, L. X., Chambers, S., Ershadi, A., et al.
789 (2017). Response of water vapour *D-excess* to land-atmosphere interactions in a semi-arid
790 environment. *Hydrology and Earth System Sciences*, *21*(1), 533-548.
791 https://doi.org/10.5194/hess-21-533-2017

792 Salamalikis, V., Argiriou, A. A., & Dotsika, E. (2015). Stable isotopic composition of
793 atmospheric water vapor in Patras, Greece: a concentration weighted trajectory approach.
794 *Atmospheric Research*, *152*, 93-104. https://doi.org/10.1016/j.atmosres.2014.02.021
795 Steen-Larsen, H. C., Johnsen, S. J., Masson-Delmotte, V., Stenni, B., Risi, C., Sodemann, H., et
796 al. (2013). Continuous monitoring of summer surface water vapor isotopic composition
797 above the Greenland Ice Sheet. *Atmospheric Chemistry and Physics*, *13*(9), 4815-4828.
798 https://doi.org/10.5194/acp-13-4815-2013
799 Steen-Larsen, H. C., Masson-Delmotte, V., Hirabayashi, M., Winkler, R., Satow, K., Prie, F., et
800 al. (2014b). What controls the isotopic composition of Greenland surface snow? *Climate of*
801 *the Past*, *10*(1), 377-392. https://doi.org/10.5194/cp-10-377-2014
802 Steen-Larsen, H. C., Sveinbjörnsdottir, A. E., Jonsson, T., Ritter, F., Bonne, J. L., Masson-
803 Delmotte, V., et al. (2015). Moisture sources and synoptic to seasonal variability of North
804 Atlantic water vapor isotopic composition. *Journal of Geophysical Research: Atmospheres*,
805 *120*(12), 5757-5774. https://doi.org/10.1002/2015jd023234
806 Steen-Larsen, H. C., Sveinbjornsdottir, A. E., Peters, A. J., Masson-Delmotte, V., Guishard, M.
807 P., Hsiao, G., et al. (2014a). Climatic controls on water vapor deuterium excess in the
808 marine boundary layer of the North Atlantic based on 500 days of in situ, continuous
809 measurements. *Atmospheric Chemistry and Physics*, *14*(15), 7741-7756.
810 https://doi.org/10.5194/acp-14-7741-2014
811 Sturm, P., & Knohl, A. (2010). Water vapor δ^2H and δ^{18}O measurements using off-axis
812 integrated cavity output spectroscopy. *Atmospheric Measurement Techniques*, *3*(1), 67-77.
813 https://doi.org/10.5194/amt-3-67-2010

Tian, L. D., Yu, W. S., Schuster, P. F., Wen, R., Cai, Z. Y., Wang, D., et al. (2020). Control of seasonal water vapor isotope variations at Lhasa, southern Tibetan Plateau. *Journal of Hydrology*, *580*, 124237. https://doi.org/10.1016/j.jhydrol.2019.124237

Tremoy, G., Vimeux, F., Vimeux, F., Souley, I., Risi, C., Favreau, G., & Oi, M. (2014). Clustering mesoscale convective systems with laser-based water vapor delta O-18 monitoring in Niamey (Niger). *Journal of Geophysical Research: Atmospheres*, *119*(9), 5079-5103. https://doi.org/10.1002/2013jd020968

Uemura, R., Matsui, Y., Yoshimura, K., Motoyama, H., & Yoshida, N. (2008). Evidence of deuterium excess in water vapor as an indicator of ocean surface conditions. *Journal of Geophysical Research: Atmospheres*, *113*, D19114. https://doi.org/10.1029/2008jd010209

Vuille, M., Bradley, R. S., Werner, M., Healy, R., & Keimig, F. (2003). Modeling $\delta^{18}O$ in precipitation over the tropical Americas: interannual variability and climatic controls. *Journal of Geophysical Research: Atmospheres*, *108*(D6), 4174. https://doi.org/10.1029/2001jd002038

Wang, G. D., Wang, M., Lu, X. G., & Jiang, M. (2016). Surface elevation change and susceptibility of coastal wetlands to sea level rise in Liaohe Delta, China. *Estuarine Coastal and Shelf Science*, *180*, 204-211. https://doi.org/10.1016/j.ecss.2016.07.011

Wang, G. Y., Lan, H. M., & Liu, Z. F. (2021). Stable isotope record of super typhoon Lekima (2019). *Atmospheric Research*, *264*, 264, 105822. https://doi.org/10.1016/j.atmosres.2021.105822

Wei, Z. W., & Lee, X. H. (2019). The utility of near-surface water vapor deuterium excess as an indicator of atmospheric moisture source. *Journal of Hydrology*, *577*, 123923. https://doi.org/10.1016/j.jhydrol.2019.123923

Wei, Z. W., Yoshimura, K., Okazaki, A., Kim, W., Liu, Z. F., & Yokoi, M. (2015). Partitioning of evapotranspiration using high-frequency water vapor isotopic measurement over a rice paddy field. *Water Resources Research*, *51*(5), 3716-3729. https://doi.org/10.1002/2014wr016737

Welp, L. R., Lee, X. H., Griffis, T. J., Wen, X. F., Xiao, W., Li, S. G., et al. (2012). A meta-analysis of water vapor deuterium-excess in the midlatitude atmospheric surface layer. *Global Biogeochemical Cycles*, *26*, GB3021. https://doi.org/10.1029/2011gb004246

Wen, X. F., Lee, X. H., Sun, X. M., Wang, J. L., Hu, Z. M., Li, S.G., & Yu, G.R. (2012). Dew water isotopic ratios and their relationships to ecosystem water pools and fluxes in a cropland and a grassland in China. *Oecologia*, *168*(2), 549-561. https://doi.org/10.1007/s00442-011-2091-0

Wen, X. F., Sun, X. M., Zhang, S. C., Yu, G. R., Sargent, S. D., & Lee, X. H. (2008). Continuous measurement of water vapor D/H and $^{18}O/^{16}O$ isotope ratios in the atmosphere. *Journal of Hydrology*, *349*(3-4), 489-500. https://doi.org/10.1016/j.jhydrol.2007.11.021

Wen, X. F., Zhang, S. C., Sun, X. M., Yu, G. R., & Lee, X. H. (2010). Water vapor and precipitation isotope ratios in Beijing, China. *Journal of Geophysical Research: Atmospheres*, *115*, D1103. https://doi.org/10.1029/2009jd012408

Wu, H. W, Li, X. Y., Zhang, J. M., Li, J., Liu, J. Z., Tian, L. H., & Fu, C.S. (2019). Stable isotopes of atmospheric water vapour and precipitation in the northeast Qinghai-Tibetan Plateau. *Hydrological Processes*, *33*(23), 2997-3009. https://doi.org/10.1002/hyp.13541

Wu, X. X., Chen, F. L., Liu, X. Y, Wang, S. J., Zhang, M. J., Zhu, G. F., et al. (2021). The significance of hydrogen and oxygen stable isotopes in the water vapor source in Dingxi area. *Water*, *13*(17), 2374. https://doi.org/10.3390/w13172374

Xiao, W., Lee, X. H., Hu, Y. B., Liu, S. D., Wang, W., Wen, X. F., et al. (2017). An experimental investigation of kinetic fractionation of open-water evaporation over a large lake. *Journal of Geophysical Research: Atmospheres*, *122*(21), 11651-11663. https://doi.org/10.1002/2017jd026774

Xu, T., Pang, H. X., Zhan, Z. J., Zhang, W. B., Guo, H. W., Wu, S. Y., & Hou, S. G. (2022). Water vapor isotopes indicating rapid shift among multiple moisture sources for the 2018-2019 winter extreme precipitation events in southeastern China. *Hydrology and Earth System Sciences*, *26*(1), 117-127. https://doi.org/10.5194/hess-26-117-2022

Zhang, S. C., Sun X. M., Wang J. L., Yu, G. R., Wen, X. F. (2011). Short-term variations of vapor isotope ratios reveal the influence of atmospheric processes. *Journal of Geographical Sciences*, *21*(3), 401-416. https://doi.org/10.1007/s11442-011-0853-6

Zhao, L., Wang, L., Liu, X., Xiao, H., Ruan, Y., & Zhou, M. (2014). The patterns and implications of diurnal variations in the d-excess of plant water, shallow soil water and air moisture. *Hydrology and Earth System Sciences*, *18*(10), 4129-4151. https://doi.org/10.5194/hess-18-4129-2014